

LETTER TO THE EDITOR

Herschel observations of the hydroxyl radical (OH) in young stellar objects[★]

S.F. Wampfler¹, G.J. Herczeg², S. Bruderer¹, A.O. Benz¹, E.F. van Dishoeck^{2,3}, L.E. Kristensen³, R. Visser³,
S.D. Doty⁴, M. Melchior^{1,5}, T.A. van Kempen⁶, U.A. Yıldız³, C. Dedes¹, J.R. Goicoechea⁷, A. Baudry⁸,
G. Melnick⁶, R. Bachiller⁹, M. Benedettini¹⁰, E. Bergin¹¹, P. Bjerkeli¹², G.A. Blake¹³, S. Bontemps⁸, J. Braine⁸,
P. Caselli^{14,15}, J. Cernicharo⁷, C. Codella¹⁵, F. Daniel⁷, A.M. di Giorgio¹⁰, C. Dominik^{16,17}, P. Encrenaz¹⁸,
M. Fich¹⁹, A. Fuente²⁰, T. Giannini²¹, Th. de Graauw²², F. Helmich²², F. Herpin⁸, M.R. Hogerheijde³, T. Jacq⁸,
D. Johnstone^{23,24}, J.K. Jørgensen²⁵, B. Larsson²⁶, D. Lis²⁷, R. Liseau¹², M. Marseille²², C. McCoey^{19,28},
D. Neufeld²⁹, B. Nisini²¹, M. Olberg¹², B. Parise³⁰, J.C. Pearson³¹, R. Plume³², C. Risacher²²,
J. Santiago-García³³, P. Saraceno¹⁰, R. Shipman²², M. Tafalla⁹, F.F.S. van der Tak^{22,34}, F. Wyrowski³⁰,
P. Roelfsema²², W. Jellema²², P. Dieleman²², E. Caux^{35,36}, and J. Stutzki³⁷

(Affiliations can be found after the references)

January 23, 2018

ABSTRACT

Aims. ‘Water in Star-forming regions with *Herschel*’ (WISH) is a *Herschel* Key Program investigating the water chemistry in young stellar objects (YSOs) during protostellar evolution. Hydroxyl (OH) is one of the reactants in the chemical network most closely linked to the formation and destruction of H₂O. High-temperature ($T \gtrsim 250$ K) chemistry connects OH and H₂O through the $\text{OH} + \text{H}_2 \rightleftharpoons \text{H}_2\text{O} + \text{H}$ reactions. Formation of H₂O from OH is efficient in the high-temperature regime found in shocks and the innermost part of protostellar envelopes. Moreover, in the presence of UV photons, OH can be produced from the photo-dissociation of H₂O through $\text{H}_2\text{O} + \gamma_{\text{UV}} \Rightarrow \text{OH} + \text{H}$.

Methods. High-resolution spectroscopy of the 163.12 μm triplet of OH towards HH 46 and NGC 1333 IRAS 2A was carried out with the Heterodyne Instrument for the Far Infrared (HIFI) on board the *Herschel Space Observatory*. The low- and intermediate-mass protostars HH 46, TMR 1, IRAS 15398-3359, DK Cha, NGC 7129 FIRS 2, and NGC 1333 IRAS 2A were observed with the Photodetector Array Camera and Spectrometer (PACS) on *Herschel* in four transitions of OH and two [O I] lines.

Results. The OH transitions at 79, 84, 119, and 163 μm and [O I] emission at 63 and 145 μm were detected with PACS towards the class I low-mass YSOs as well as the intermediate-mass and class I Herbig Ae sources. No OH emission was detected from the class 0 YSO NGC 1333 IRAS 2A, though the 119 μm was detected in absorption. With HIFI, the 163.12 μm was not detected from HH 46 and only tentatively detected from NGC 1333 IRAS 2A. The combination of the PACS and HIFI results for HH 46 constrains the line width ($\text{FWHM} \gtrsim 11 \text{ km s}^{-1}$) and indicates that the OH emission likely originates from shocked gas. This scenario is supported by trends of the OH flux increasing with the [O I] flux and the bolometric luminosity, as found in our sample. Similar OH line ratios for most sources suggest that OH has comparable excitation temperatures despite the different physical properties of the sources.

Key words. Astrochemistry — Stars: formation — ISM: molecules — ISM: jets and outflows — ISM: individual objects: HH 46

1. Introduction

The hydroxyl radical (OH) is a cornerstone species of the oxygen chemistry in dense clouds and is particularly important in the chemical reaction network of water. H₂O and OH are closely linked through the $\text{OH} + \text{H}_2 \rightleftharpoons \text{H}_2\text{O} + \text{H}$ reactions. The formation path of H₂O from OH is efficient at the high temperatures found in shocks or in the innermost parts of circumstellar envelopes (Kaufman & Neufeld 1996; Charnley 1997). Below about 250 K, standard gas-phase chemistry applies, in which H₂O is formed and destroyed through ion-molecule reactions. In regions not completely shielded from UV radiation, photo-dissociation becomes a major destruction path of H₂O, leaving

OH as a byproduct. A better understanding of the OH emission will therefore help to constrain the water chemistry.

The observation of far-infrared (FIR) rotational OH lines by ground based facilities is severely limited by the Earth’s atmosphere. Previous studies of OH FIR emission with the Infrared Space Observatory (ISO) showed that OH is one of the major molecular coolants in star-forming regions (e.g. Giannini et al. 2001). However, with a large beam of 80”, ISO was unable to resolve the central source from the outflows, preventing an assessment of the origin of the OH emission. Interpretation of the ISO OH measurements thus relied mostly on the assumption that the OH emission arises from gas with the same temperature and density as the high-J CO FIR emission (e.g. Nisini et al. 1999; Ceccarelli et al. 1998). The *Herschel Space Observatory* permits observations of OH FIR transitions at both higher angular and spectral resolution and at higher sensitivity than ISO.

[★] *Herschel* is an ESA space observatory with science instruments provided by European-led Principal Investigator consortia and with important participation from NASA.

Observations of H₂O, OH and related species towards a large set of young stellar objects over a wide range of luminosities and masses are being carried out in the ‘Water In Star-forming regions with *Herschel*’ (WISH) key program to trace the water chemistry during protostellar evolution (van Dishoeck et al. in prep). OH emission at 163.12 μm (1837.8 GHz) was detected with PACS towards the class I YSO HH 46 (van Kempen et al. 2010b), but the triplet, split by 90 MHz, could not be resolved. Based on modeling results, the OH emission was attributed to a *J*-type shock and not to the quiescent envelope. We carried out high-resolution spectroscopy with HIFI to test whether the detected OH emission is dominated by shock contribution by resolving the line profiles. This paper presents the HIFI observations in HH 46 as well as the class 0 object NGC 1333 IRAS 2A. New PACS observations of OH and [O I] are reported for the low-mass protostars IRAS 15398-3359, NGC 1333 IRAS 2A, and TMR 1.

2. Observations and data reduction

Because of spin-orbit interaction, the OH rotational levels are built within two ladders, $^2\Pi_{3/2}$ and $^2\Pi_{1/2}$ (Offer & van Dishoeck 1992). Each level is further split by Λ doubling and hyperfine structure. A level diagram can be found in Fig. B.1 in the appendix. We use the molecular data from the Leiden atomic and molecular database LAMDA¹ (Schöier et al. 2005).

High-resolution observations of the OH triplet at 163.12 μm (1837.747, 1837.817 and 1837.837 GHz) were performed with the Heterodyne Instrument for the Far-Infrared (HIFI, De Graauw et al. 2010) on board the ESA *Herschel Space Observatory* (Pilbratt et al. 2010) towards HH 46 and NGC 1333 IRAS 2A. HIFI data were stitched together using the Herschel Interactive Processing Environment (HIPE v3.0.1, Ott 2010) and further analyzed using GILDAS-CLASS² software. We removed standing waves after the subtraction of a low-order polynomial and calibrated to T_{mb} scale using a main beam efficiency of 0.74. The H and V polarizations were combined.

HH 46, TMR 1, IRAS 15398-3359, and NGC 7129 FIRS 2 were observed with PACS (Poglitsch et al. 2010) in line spectroscopy mode around four OH doublets at 79, 84, 119, and 163 μm . The [O I] 63 and 145.5 μm lines were also observed except for TMR 1. Each segment at $\lambda < 100 \mu\text{m}$ and $\lambda > 100 \mu\text{m}$ covers 1 and 2 μm at $R \sim 3000$ and $R \sim 1500$, respectively. In addition, DK Cha and NGC 1333 IRAS 2A were observed with PACS from 55–210 μm at $R \sim 1000$ in range spectroscopy mode. Details of the PACS observations of HH 46, NGC 7129 FIRS 2, and DK Cha are described in van Kempen et al. (2010b), Fich et al. (2010), and van Kempen et al. (2010a), respectively. All spectra were reduced with HIPE v2.9. PACS spectra are recorded in a 5×5 array of 9.4 square spatial pixels (spaxels). The observations of IRAS 15398-3359, TMR 1, NGC1333 IRAS 2A, and DK Cha were mispointed sufficiently in a way that the peak of the continuum emission differs from the central spaxel.

The line and continuum emission seen by PACS is spatially extended in most cases. Spectra were extracted from the spaxels that include OH emission. The wavelength-dependent point-spread function was roughly corrected by comparing the amount of continuum emission in the summed spaxels to that in the total array. Most integrated line intensities were derived from Gaussian fits to the unresolved lines. In a few cases, the OH

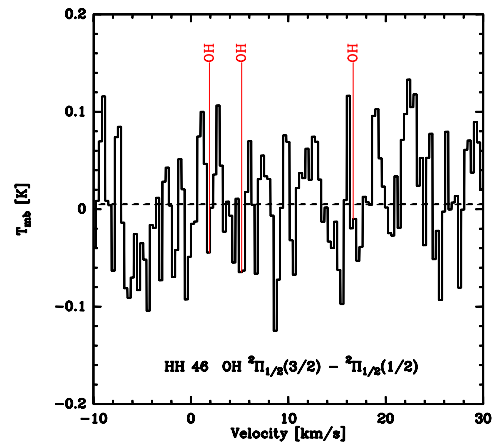


Fig. 1. HIFI spectrum at 163.12 μm (1837.8 GHz) towards the low-mass YSO HH 46 ($v_{\text{lsr}} = 5.2 \text{ km s}^{-1}$). OH lines were not detected in 34 min of on source integration time (polarizations combined).

doublets could not be resolved and the intensities were then derived by simple integration over the spectrum. The absolute flux calibration below and above 100 μm was separately determined from in-flight observations of (point) calibration sources. The relative spectral response function within each band was determined from ground calibration prior to launch. The uncertainty in absolute and relative fluxes is estimated to be 30-50%. Additional details on the observations can be found in the appendix.

3. Results

HIFI did not detect the 163.12 μm OH hyperfine triplet at the noise level of $T_{\text{rms}} \approx 70 \text{ mK}$ on T_{mb} scale for the nominal WBS resolution of about 1.1 MHz (0.163 km s^{-1}). The spectrum is presented in Fig. 1. Combining the HIFI and PACS observations constrains the line width (see Sect. 4).

PACS detected OH emission at 79, 84, 119, and 163 μm towards the class I sources HH 46, TMR 1 and IRAS 15398-3359 as well as the class I Herbig Ae star DK Cha and the intermediate-mass source NGC 7129 FIRS 2 (Fig. 2). An exception is the 163.40 μm line of HH 46, where we only have an upper limit because of the uncertain baseline towards the end of the spectral window where the line is located. The [O I] 63 μm and 145 μm lines were also detected. An overview of the results is given in Table 1. The 1σ errors listed in Table 1 do not include the systematic error of 30-50% from uncertainty in the calibration. Because of blending with CO(31-30), the 84.42 μm doublet component of OH is not listed. For the analysis, we assumed the flux to be identical to the 84.60 μm OH flux because all observed doublets show comparable fluxes of the components within the calibration uncertainty.

The only class 0 YSO in the sample, NGC 1333 IRAS 2A, is fundamentally different from all other sources in the sample. The OH 119 μm doublet is seen in absorption, with an equivalent width of about 7.5 km s^{-1} for each component. No other OH lines were detected at the noise level obtained after removal of the fringing effects. However, the upper limits are larger than the fluxes detected from the class I sources. On the other hand, the upper limit on the [O I] 63 μm emission is at least a factor of four lower than the weakest [O I] 63 μm line found in our sample.

¹ <http://www.strw.leidenuniv.nl/~moldata/>

² <http://www.iram.fr/IRAMFR/GILDAS>

Table 1. OH and [O I] line fluxes observed with PACS.

Transition	λ [μm]	ν [GHz]	E_{up} [K]	HH 46	TMR 1	IRAS 15398	DK Cha	NGC 7129	N 1333 I 2A
				Flux [$10^{-18} \text{ W m}^{-2}$]	Flux [$10^{-18} \text{ W m}^{-2}$]	Flux [$10^{-18} \text{ W m}^{-2}$]	Flux [$10^{-18} \text{ W m}^{-2}$]	Flux [$10^{-18} \text{ W m}^{-2}$]	Flux [$10^{-18} \text{ W m}^{-2}$]
OH $_{1,1} - _{0,0}$	79.12	3789.3	181.9	55 ± 7	128 ± 14	194 ± 29^a	360 ± 87	229 ± 33	<350
OH $_{2,2} - _{1,1}$	79.18	3786.3	181.7	38 ± 5	102 ± 14	- ^a	315 ± 58	230 ± 39	-
OH $_{3,3} - _{2,2}$	84.60	3543.8	290.5	87 ± 6	170 ± 18	93 ± 16	347 ± 48	181 ± 28	<165
OH $_{4,4} - _{3,3}$	119.23	2514.3	120.7	38 ± 9	83 ± 10	121 ± 17	95 ± 50^a	132 ± 39	absorption
OH $_{5,5} - _{4,4}$	119.44	2510.0	120.5	44 ± 7	101 ± 11	130 ± 17	-	134 ± 59	absorption
OH $_{6,6} - _{5,5}$	163.12	1837.8	270.1	22 ± 4	56 ± 8	47 ± 9	170 ± 60^a	116 ± 45	<100
OH $_{7,7} - _{6,6}$	163.40	1834.7	269.8	<27	55 ± 7	54 ± 10	- ^a	69 ± 26	-
[O I] $^3\text{P}_1 - ^3\text{P}_2$	63.18	4744.8	227.7	1260 ± 54	-	1958 ± 197	3128 ± 333	1219 ± 130	<320
[O I] $^3\text{P}_0 - ^3\text{P}_2$	145.53	2060.1	326.6	82 ± 8	-	122 ± 17	170 ± 72	104 ± 35	<180

^a Doublet not resolved. Table lists the integrated flux over both components.

4. Analysis

To constrain the line width of the 163.12 μm OH triplet from HH 46, the HIFI non-detection is combined with the flux ($22 \times 10^{-18} \text{ W m}^{-2}$) of the unresolved lines measured with the high-sensitivity PACS instrument. The expected integrated intensity for HIFI is $\sim 1.1 \text{ K km s}^{-1}$ for the triplet in total, as calculated from the PACS observation. This value was derived for a $13''$ beam under the assumption that the source is unresolved, because the OH emission from HH 46 appears to be centrally concentrated (van Kempen et al. 2010b). Assuming LTE ratios ($\sim A_{ul}g_u$) for the three components, the strongest transition has an integrated intensity of 0.66 K km s^{-1} . An upper limit on the integrated intensity is calculated from the HIFI observation using $\sigma = 1.3 \sqrt{\delta\nu \Delta\nu} T_{\text{rms}}$ with $\delta\nu$ the velocity resolution, $\Delta\nu$ the expected line width and an assumed 30 % calibration uncertainty. Rebinning the spectrum to a resolution of 16 MHz (2.6 km s^{-1}) yields an rms of 31 mK and would therefore allow 5σ (3σ) detections for Gaussian lines with FWHM $\leq 4 \text{ km s}^{-1}$ (FWHM $\leq 11 \text{ km s}^{-1}$). From the non-detection we conclude that the flux observed with PACS is likely to be emitted from lines with FWHM $\gtrsim 11 \text{ km s}^{-1}$. For comparison, the FWHM of the $\text{H}_2\text{O } 1_{10} - 1_{01}$ transition derived from recent unpublished HIFI observations is about 16 km s^{-1} . The CO(6-5) and CO(7-6) lines observed with APEX by van Kempen et al. (2009) are narrower.

In a similar HIFI observation, OH emission was tentatively detected below the 5σ level for the strongest triplet component in NGC 1333 IRAS 2A, in agreement with the upper limits on OH emission in the PACS observation of the same source. Given the uncertain baseline, this needs to be treated with caution.

Figure 3 compares the OH fluxes from YSOs as measured here with PACS and in ISO observations of two additional sources, Ser SMM1 (Larsson et al. 2002) and NGC 1333 IRAS 4 (Giannini et al. 2001). Despite the wide range of luminosities and masses covered in our sample, the sources show surprisingly similar characteristics in terms of their OH emission: the OH 84 μm doublet is generally the strongest of the four, while the integrated intensity of the weakest doublet at 163 μm is roughly a factor of three lower. The 119 μm flux can vary compared to higher excitation lines because this line, which is connected to the ground state level, becomes more easily optically thick. It can also be affected by absorption against the continuum by cold gas layers lying in front of the source. The 79 μm doublet links the lowest energy states of both rotational ladders, but because of the smaller Einstein A coefficients of the cross-ladder transitions, these lines are less affected by optical depth than the 119 μm lines. The 79 μm fluxes are lower than those at 84 μm for most sources, but higher than at 119 μm .

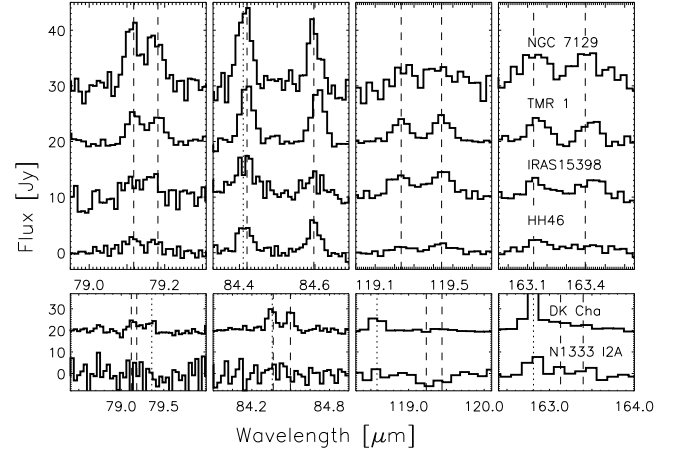


Fig. 2. PACS spectra of the observed OH doublets at 79, 84, 119, and 163 μm . Sources in the top panel were observed in line spectroscopy mode, those in the lower panel in range spectroscopy mode (different sampling). Dashed vertical lines indicate the OH frequencies, dotted lines show the position of CO lines.

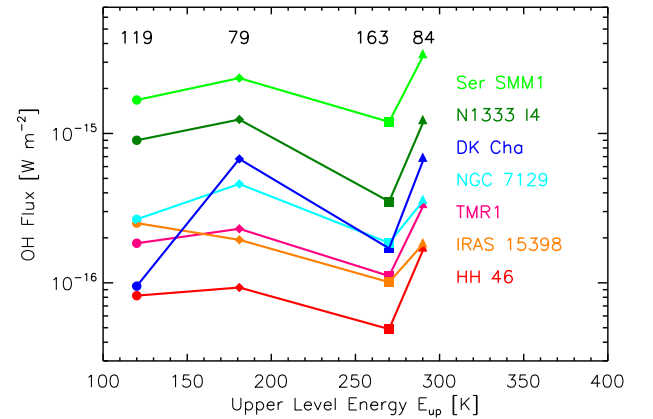


Fig. 3. Observed OH line fluxes from PACS plotted versus the upper level energy of the transition. Ser SMM 1 and NGC 1333 IRAS 4 measured with ISO are included for comparison. Symbols correspond to different OH transitions: 79 μm as diamond, 84 μm as triangle, 119 μm as circle, and 163 μm as square. Fluxes of the doublet components are summed. The 84.60 μm flux multiplied by two is used for the 84 μm doublet because the 84.42 μm line is blended with CO(31-30).

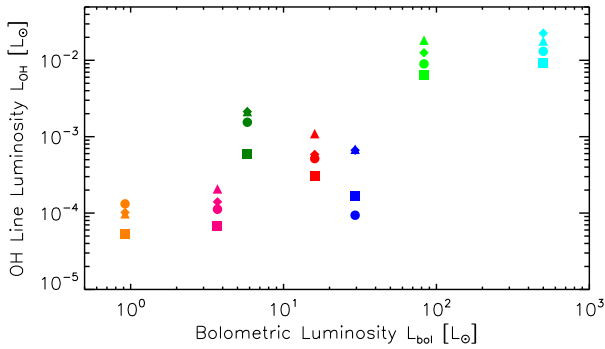


Fig. 4. Dependence of OH line luminosity on the bolometric luminosity of the source. Symbols and colors as in Fig. 3.

Flux ratios of the observed OH lines were calculated from the summed doublet components to compare the excitation of the involved energy levels among the sources. The line ratios of different sources agree within a factor of two except when the $119\ \mu\text{m}$ transition is involved (Fig. C.1 in the appendix) and are consistent with the results from ISO observations from the class 0 sources NGC 1333 IRAS 4 and Ser SMM1.

Emission in the $84\ \mu\text{m}$ transition, which has $E_{\text{up}}/k_B \approx 300\ \text{K}$, indicates that OH is tracing the warm ($T \gtrsim 100\ \text{K}$) and dense ($n \gtrsim 10^5\ \text{cm}^{-3}$) gas in our sources. Modeling results show that transitions in the $^2\Pi_{3/2}$ ladder are mostly excited by collisions while the population of the $^2\Pi_{1/2}$ levels is dominated by radiative pumping via the cross-ladder transitions. The weak $163\ \mu\text{m}$ lines and emission at $79\ \mu\text{m}$ indicate that FIR pumping is less important than collisional excitation in our sources.

Figure 4 shows the trend of stronger OH emission with increasing bolometric source luminosity L_{bol} found in our source sample. We calculated the OH line luminosity L_{OH} individually for each transition and source from the observed fluxes and found indications that the differences between the sources may depend on the individual L_{bol} . The correlation between L_{OH} and L_{bol} is reminiscent of that found for the CO outflow force with luminosity (Bontemps et al. 1996). The latter relation was taken as evidence that more massive envelopes have higher accretion rates and thus drive more powerful outflows. van Kempen et al. (2010b) speculate that the OH emission originates in the wake of the jet impinging on the dense, inner parts of the envelope, creating dissociative shocks in which [O I] is the dominant coolant, followed by OH (Neufeld & Dalgarno 1989). The relation between OH emission and luminosity supports this scenario.

Comparison of OH with [O I] emission shows that stronger OH emission coincides with higher [O I] intensities (Fig. 5) and also with increasing [O I] $63/145\ \mu\text{m}$ line flux ratios. For HH 46, TMR 1, and NGC 7129 FIRS 2, the bulk of the [O I] and OH emission comes from close to the protostar where densities are on the order of $10^5\ \text{cm}^{-3}$ or higher, as illustrated by the lack of extended OH emission in HH 46 (van Kempen et al. 2010b). Some spatially extended OH emission is detected from IRAS 15398-3359 and DK Cha, and is highly correlated with the spatial extent of [O I] emission. The correlation between the intensities (Fig. 5) suggests that the bulk of [O I] and OH emission originates in the same physical component in all sources. This argument, together with the OH – L_{bol} and OH – [O I] relations, supports the dissociative shock scenario. The [O I] $63\ \mu\text{m} / 145\ \mu\text{m}$ line ratios are in the range of 13–19, also consistent with fast, dissociative J -type shocks ($v > 60\ \text{km s}^{-1}$, Neufeld & Dalgarno 1989). Note that an OH – [O I] relation can

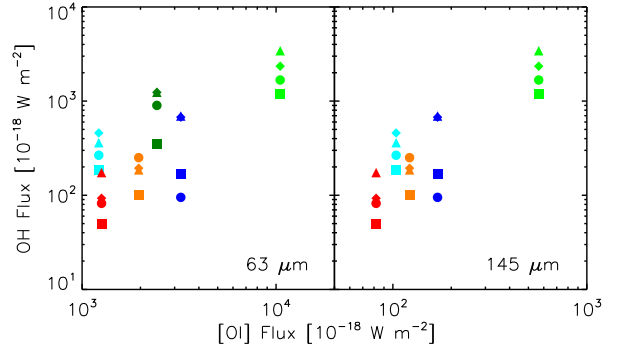


Fig. 5. Observed OH fluxes plotted against [O I] $63\ \mu\text{m}$ flux (left panel) and $145\ \mu\text{m}$ flux (right panel). Symbols and colors as in Fig. 3.

also be indicative of photo-dissociation, as argued for Sgr B2 by Goicoechea et al. (2004). Models of photon-dominated regions (Kaufman et al. 1999) predict similar [O I] $63\ \mu\text{m} / 145\ \mu\text{m}$ line ratios, but those require $n < 10^5\ \text{cm}^{-3}$, which is inconsistent with an origin in the inner, dense envelope.

5. Conclusions

The OH hyperfine transition triplet at $163.12\ \mu\text{m}$ (1837.8 GHz) was not detected above the noise level obtained with HIFI. Combined with the flux derived from the unresolved line observed with PACS, this constrains the line width to $\text{FWHM} \gtrsim 11\ \text{km s}^{-1}$. This width is much broader than expected for the quiescent envelope from ground-based observations (van Kempen et al. 2009) and indicates that the observed OH emission most likely stems from shocked gas in HH 46.

Herschel PACS observations of OH lines at 79 , 84 , 119 , and $163\ \mu\text{m}$ have been carried out for four low-mass YSOs, one intermediate-mass protostar and one class I Herbig Ae object. OH emission is detected in all sources except the class 0 YSO NGC 1333 IRAS 2A, where the OH $119\ \mu\text{m}$ transitions are observed in absorption and only upper limits can be derived for the other lines. Sources with detected OH emission show surprisingly similar OH line ratios despite the large ranges of physical properties covered in this study, suggesting that OH emission might arise from gas at similar conditions in all sources. Furthermore, we find trends of correlations between OH integrated intensities and [O I] emission as well as bolometric luminosity, consistent with an origin in the wake of dissociative shocks. Given the low number of sources in the sample, confirmation from additional observations is needed.

Further OH observations and modeling should eventually allow the determination of the OH/ H_2O abundance ratio in shocks, which traces the UV field through its dependence on the fraction of atomic to molecular hydrogen.

References

- Bontemps, S., Andre, P., Terebey, S., & Cabrit, S. 1996, *A&A*, 311, 858
- Ceccarelli, C., Caux, E., White, G. J., et al. 1998, *A&A*, 331, 372
- Charney, S. B. 1997, *ApJ*, 481, 396
- De Graauw, T., Helmich, F. P., Philipps, T. G., et al. 2010, submitted to this issue
- Fich, M., Johnstone, D., van Kempen, T. A., et al. 2010, *A&A* in press
- Giannini, T., Nisini, B., & Lorenzetti, D. 2001, *ApJ*, 555, 40
- Goicoechea, J. R., Rodríguez-Fernández, N. J., & Cernicharo, J. 2004, *ApJ*, 600, 214
- Kaufman, M. J. & Neufeld, D. A. 1996, *ApJ*, 456, 611

- Kaufman, M. J., Wolfire, M. G., Hollenbach, D. J., & Luhman, M. L. 1999, *ApJ*, 527, 795
- Larsson, B., Liseau, R., & Men'shchikov, A. B. 2002, *A&A*, 386, 1055
- Neufeld, D. A. & Dalgarno, A. 1989, *ApJ*, 344, 251
- Nisini, B., Benedettini, M., Giannini, T., et al. 1999, *A&A*, 350, 529
- Offer, A. R. & van Dishoeck, E. F. 1992, *MNRAS*, 257, 377
- Ott, S. 2010, in *ASP Conference Series, Astronomical Data Analysis Software and Systems XIX*, Y. Mizumoto, K.-I. Morita, and M. Ohishi, eds., in press.
- Schöier, F. L., van der Tak, F. F. S., van Dishoeck, E. F., & Black, J. H. 2005, *A&A*, 432, 369
- van Kempen, T. A., Green, J. D., Evans, N. J., et al. 2010a, *A&A* in press
- van Kempen, T. A., Kristensen, L. E., Herczeg, G. J., et al. 2010b, *A&A* in press
- van Kempen, T. A., van Dishoeck, E. F., Güsten, R., et al. 2009, *A&A*, 501, 633
-
- 1 Institute for Astronomy, ETH Zurich, 8093 Zurich, Switzerland
 - 2 Max Planck Institut für Extraterrestrische Physik, Giessenbachstrasse 1, 85748 Garching, Germany
 - 3 Leiden Observatory, Leiden University, PO Box 9513, 2300 RA Leiden, The Netherlands
 - 4 Department of Physics and Astronomy, Denison University, Granville, OH, 43023, USA
 - 5 Institute of 4D Technologies, University of Applied Sciences NW, CH-5210 Windisch, Switzerland
 - 6 Harvard-Smithsonian Center for Astrophysics, 60 Garden Street, MS 42, Cambridge, MA 02138, USA
 - 7 Centro de Astrobiología. Departamento de Astrofísica. CSIC-INTA. Carretera de Ajalvir, Km 4, Torrejón de Ardoz. 28850, Madrid, Spain.
 - 8 Université de Bordeaux, Laboratoire d'Astrophysique de Bordeaux, France; CNRS/INSU, UMR 5804, Floirac, France
 - 9 Observatorio Astronómico Nacional (IGN), Calle Alfonso XII,3. 28014, Madrid, Spain
 - 10 INAF - Istituto di Fisica dello Spazio Interplanetario, Area di Ricerca di Tor Vergata, via Fosso del Cavaliere 100, 00133 Roma, Italy
 - 11 Department of Astronomy, The University of Michigan, 500 Church Street, Ann Arbor, MI 48109-1042, USA
 - 12 Department of Radio and Space Science, Chalmers University of Technology, Onsala Space Observatory, 439 92 Onsala, Sweden
 - 13 California Institute of Technology, Division of Geological and Planetary Sciences, MS 150-21, Pasadena, CA 91125, USA
 - 14 School of Physics and Astronomy, University of Leeds, Leeds LS2 9JT, UK
 - 15 INAF - Osservatorio Astrofisico di Arcetri, Largo E. Fermi 5, 50125 Firenze, Italy
 - 16 Astronomical Institute Anton Pannekoek, University of Amsterdam, Kruislaan 403, 1098 SJ Amsterdam, The Netherlands
 - 17 Department of Astrophysics/IMAPP, Radboud University Nijmegen, P.O. Box 9010, 6500 GL Nijmegen, The Netherlands
 - 18 LERMA and UMR 8112 du CNRS, Observatoire de Paris, 61 Av. de l'Observatoire, 75014 Paris, France
 - 19 University of Waterloo, Department of Physics and Astronomy, Waterloo, Ontario, Canada
 - 20 Observatorio Astronómico Nacional, Apartado 112, 28803 Alcalá de Henares, Spain
 - 21 INAF - Osservatorio Astronomico di Roma, 00040 Monte Porzio catone, Italy
 - 22 SRON Netherlands Institute for Space Research, PO Box 800, 9700 AV, Groningen, The Netherlands
 - 23 National Research Council Canada, Herzberg Institute of Astrophysics, 5071 West Saanich Road, Victoria, BC V9E 2E7, Canada
 - 24 Department of Physics and Astronomy, University of Victoria, Victoria, BC V8P 1A1, Canada
 - 25 Centre for Star and Planet Formation, Natural History Museum of Denmark, University of Copenhagen, Øster Voldgade 5-7, DK-1350 Copenhagen K., Denmark
 - 26 Department of Astronomy, Stockholm University, AlbaNova, 106 91 Stockholm, Sweden
 - 27 California Institute of Technology, Cahill Center for Astronomy and Astrophysics, MS 301-17, Pasadena, CA 91125, USA
 - 28 the University of Western Ontario, Department of Physics and Astronomy, London, Ontario, N6A 3K7, Canada
 - 29 Department of Physics and Astronomy, Johns Hopkins University, 3400 North Charles Street, Baltimore, MD 21218, USA
 - 30 Max-Planck-Institut für Radioastronomie, Auf dem Hügel 69, 53121 Bonn, Germany
 - 31 Jet Propulsion Laboratory, California Institute of Technology, Pasadena, CA 91109, USA
 - 32 Department of Physics and Astronomy, University of Calgary, Calgary, T2N 1N4, AB, Canada
 - 33 Instituto de Radioastronomía Milimétrica (IRAM), Avenida Divina Pastora 7, Núcleo Central, E-18012 Granada, Spain
 - 34 Kapteyn Astronomical Institute, University of Groningen, PO Box 800, 9700 AV, Groningen, The Netherlands
 - 35 Centre d'Etude Spatiale des Rayonnements, Université de Toulouse [UPS], 31062 Toulouse Cedex 9, France
 - 36 CNRS/INSU, UMR 5187, 9 avenue du Colonel Roche, 31028 Toulouse Cedex 4, France
 - 37 KOSMA, I. Physik. Institut, Universität zu Köln, Zùlpicher Str. 77, D 50937 Köln, Germany

Acknowledgements. The work on star formation at ETH Zurich is partially funded by the Swiss National Science Foundation (grant nr. 200020-113556). This program is made possible thanks to the Swiss HIFI guaranteed time program. HIFI has been designed and built by a consortium of institutes and university departments from across Europe, Canada and the United States under the leadership of SRON Netherlands Institute for Space Research, Groningen, The Netherlands and with major contributions from Germany, France and the US. Consortium members are: Canada: CSA, U. Waterloo; France: CESR, LAB, LERMA, IRAM; Germany: KOSMA, MPIfR, MPS; Ireland, NUI Maynooth; Italy: ASI, IFSI-INAF, Osservatorio Astrofisico di Arcetri- INAF; Netherlands: SRON, TUD; Poland: CAMK, CBK; Spain: Observatorio Astronómico Nacional (IGN), Centro de Astrobiología (CSIC-INTA). Sweden: Chalmers University of Technology - MC2, RSS & GARD; Onsala Space Observatory; Swedish National Space Board, Stockholm University - Stockholm Observatory; Switzerland: ETH Zurich, FHNW; USA: Caltech, JPL, NHSC.

Appendix A: Observational details

Table A.1 lists the coordinates, observing dates, and the observation identity numbers of our sources along with the assumed distance, the bolometric luminosity, the envelope mass and the source type. For comparison, Ser SMM1 and NGC 1333 IRAS 4 observed with ISO are included as well. For Ser SMM1, we use the average values of the fluxes presented by Larsson et al. (2002). The data for NGC 1333 IRAS 4 are taken from Giannini et al. (2001). Note that for NGC 1333 IRAS 4, we use the luminosity and mass of NGC 1333 IRAS 4A.

Table A.1. Source properties and observational details.

Source	Distance [pc]	Luminosity [L_{\odot}]	Envelope Mass [M_{\odot}]	Type	RA [h m s]	Dec [$^{\circ}$ ' '']	Obs. Date	Obs.id
HH 46	450 ^a	16 ^b	5.1 ^b	Class I	08:25:43.9	-51:00:36	2009-10-26 2010-04-17	1342186315 (PACS) 1342194783 (HIFI)
TMR 1	140 ^c	3.7 ^d	0.12 ^e	Class I	04:39:13.7	+25:53:21	2010-03-29	1342192984 (PACS)
IRAS 15398-3359	130 ^f	0.92 ^g	0.5 ^h	Class I	15:43:01.3	-34:09:15	2010-02-27	1342191302 (PACS)
DK Cha	178 ⁱ	29.4 ^j	0.03 ^j	Herbig Ae	12:53:17.2	-77:07:10.6	2009-12-10 2009-12-10	1342188039 (PACS) 1342188040 (PACS)
NGC 7129 FIRS 2	1260 ^k	500 ^l	50 ^m	Intermed.-Mass	21:43:01.7	+66:03:23.6	2009-10-26	1342186321 (PACS)
NGC 1333 I 2A	235 ⁿ	20 ^o	1.0 ^o	Class 0	03:28:55.6	+31:14:37	2010-02-13 2010-02-24 2010-03-08	1342190686 (PACS) 1342191149 (PACS) 1342191773 (HIFI)
Serpens SMM1	415 ^p	82.9 ^q	8.7 ^q	Class 0			-	ISO ^r
NGC 1333 I 4	235 ⁿ	5.8 ^o	4.5 ^o	Class 0			-	ISO ^s

^a Heathcote, S., Morse, J. A., Hartigan, P., et al. 1996, AJ, 112, 1141^b van Kempen, T. A., van Dishoeck, E. F., Güsten, R. et al. 2009, A&A, 501, 633^c Motte, F., Andre, P., & Neri, R. 1998, A&A, 336, 150^d Ohashi, N., Hayashi, M., Kawabe, R. et al. 1996, ApJ, 466, 317^e Jørgensen, J. K., Schöier, F.L., & van Dishoeck, E.F. 2002, A&A, 389, 908^f Murphy, D. C., Cohen, R., & May, J. 1986, A&A, 167, 234^g Froebrich, D. 2005, ApJS, 156, 169^h van Kempen, T. A., van Dishoeck, E. F., Hogerheijde, M. R. et al., 2009, A&A, 508, 259ⁱ Whittet, D. C. B., Prusti, T., Franco, G. A. P., et al. 1997, A&A, 327, 1194^j van Kempen, T. A., Green, J. D., Evans, N. J. et al. A&A, 2010, accepted^k Shevchenko, V.S. and Yakubov, S.D. 1989, SvA, 33, 370^l Johnstone, D., Fich, M., M^cCoe, C. et al. 2010, this volume^m Crimier, N., Ceccarelli, C., Alonso-Albi, T. et al. 2010, arxiv 1005.0947ⁿ Hirota, T., Bushimata, T., Choi, Y. K., et al. 2008, PASJ, 60, 37^o Jørgensen, J. K., van Dishoeck, E. F., Visser, R., et al. 2009, A&A, 507, 861^p Dzib, S., Loinard, L., Mioduszewski, A.J., et al. 2010, ApJ, in press, arXiv1003.5900^q Hogerheijde, M. R., van Dishoeck, E. F., Salverda, J. M. et al., ApJ, 513, 350 (L_{bol} scaled to a distance of 415 pc)^r Larsson, B., Liseau, R. & Men'shchikov, A.B. 2002, A&A, 386, 1055^s Giannini, T., Nisini, B. & Lorenzetti, D. 2001, ApJ, 555, 40

Appendix B: OH term diagram

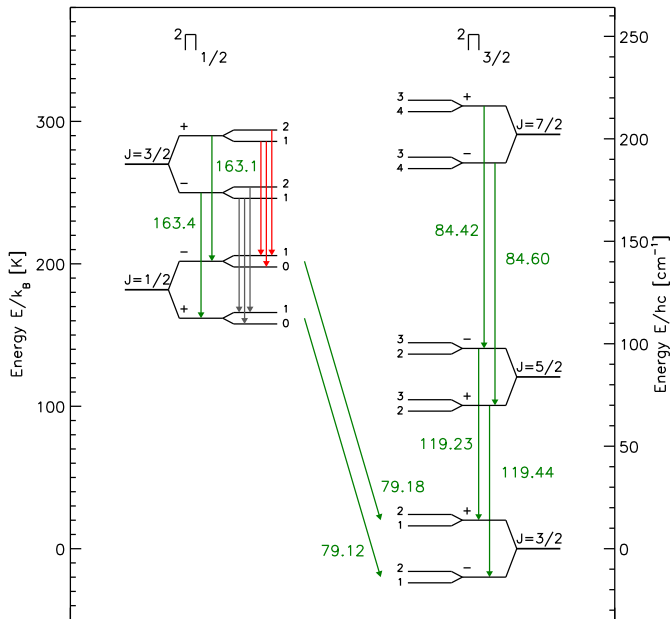


Fig. B.1. Level diagram of the lowest excited states of OH up to $E_{\text{up}} \approx 300$ K. Splitting of the levels because of Λ -doubling and hyperfine structure is not to scale. Transitions observed with PACS are shown in green, the high-resolution observations of the hyperfine transitions carried out with HIFI in red.

Appendix C: OH line ratios

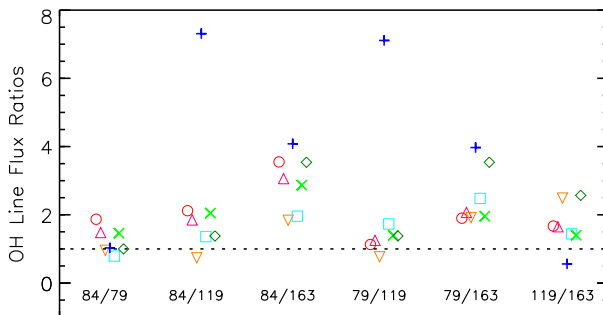


Fig. C.1. Ratios of the observed OH fluxes. The numbers denote the corresponding wavelengths. The symbols are: circle for HH 46, upward triangle for TMR 1, downward triangle for IRAS 15398-3359, squares for NGC 7129 FIRS 2, plus signs for DK Cha, crosses for Ser SMM1 and diamonds for NGC 1333 IRAS 4. The color coding is the same as in Fig. 3.